Korean J. Chem. Eng., 38(2), 342-353 (2021)
DOI: 10.1007/s11814-020-0701-4

pISSN: 0256-1115
eISSN: 1975-7220

A two-way coupled CFD-DQMOM approach for long-term dynamic simulation of a fluidized bed reactor

Minjun Kim, Kyoungmin Lee, Youngseok Bak, and Jong Min Lee†

School of Chemical and Biological Engineering, Institute of Chemical Processes, Seoul National University, Gwanak-ro 1, Gwanak-gu, Seoul 08826, Korea

(*Received 18 June 2020 • Revised 21 September 2020 • Accepted 28 October 2020*)

Abstract−For the long-term dynamic simulation of a fluidized bed reactor (FBR), a two-way coupled computational fluid dynamics (CFD)-direct quadrature method of moments (DQMOM) approach is proposed. In this approach, CFD is first used only for hydrodynamic information without simulating any other chemical reactions or physical phenomena. Subsequently, the derived information is applied to the DQMOM calculation in MATLAB. From the calculation, a particle size distribution is obtained and subsequently adopted in a new CFD model to reflect the flow change caused by a change in the particle size distribution. Through several iterative calculations, long-term dynamic simulations are performed. To evaluate the efficacy of the proposed approach, the results from the suggested approach are compared for 60 s with those of the CFD-quadrature method of moments (QMOM) approach, which calculates hydrodynamics and physical phenomena simultaneously in CFD. The proposed approach successfully simulated the FBR for 6 h. The results confirmed that the proposed method can simulate complex flow patterns, which cannot be obtained in conventional CFD models. Another advantage of the approach is that it can be applied to various industrial multiphase reactors without any tuning parameters.

Keywords: Fluidized Bed Reactor, CFD, Compartmental Model, Population Balance Model, Long-term Dynamic Simulation

INTRODUCTION

Fluidized bed reactors (FBRs) are widely used to produce polyolefins owing to their superior transfer characteristics and simple configuration [1-3]. In the FBRs, a particle is suspended and behaves as though it is a fluid by a high-velocity fluid passing through. Despite several advantages of FBRs, complex flows between a particle and fluid render their operation difficult. Consequently, analyzing the internal flow dynamics of FBRs is a main issue and a computationally feasible solution is still being sought [2-4].

Computational fluid dynamics (CFD) can calculate flow information from a simple single phase to complex multiphase hydrodynamics, which is difficult to obtain experimentally [5-8]. Owing to its advantages, CFD simulation has been widely applied to chemical reactors [9-11]. Kim et al. [12] employed CFD to simulate mineral carbonation reactions in a slurry reactor, whereas Zimmermann and Taghipour [13] applied CFD simulations to an FBR. Furthermore, Park et al. [14] integrated multi-objective Bayesian optimization with CFD and automated the task of selecting the reactor structure and optimizing operation condition.

On the other hand, the population balance model (PBM) has been studied to account for particulate phenomena in FBRs [15-18]. Among the methods to solve the PBM, the discretization population balance approach and the classes methods are direct methods that discretize the internal coordinate, e.g., the particle length, into a finite series of bins. Acceptable accuracy can be obtained if a large number of bins are used. However, a tradeoff exists between the number of bins and the computational cost, and the methods become impractical for multiphase reactors owing to the excessive number of required bins [19]. As alternative methods to efficiently solve the PBM, the quadrature method of moments (QMOM) and a direct quadrature method of moments (DQMOM) have garnered attention because both require only a few abscissas to compute particle size distribution [3,20].

Recently, much effort has been expended into analyzing FBRs through the integration of CFD and QMOM/DQMOM [18,21,22]. However, the studies involved short-term simulations because exorbitant computational costs are required in CFD simulations to simulate the hydrodynamics and kinetics or the PBM simultaneously. For long-term CFD simulation, CFD-based compartmental models have been studied by various research groups [23-28]. In those models, a reactor is first divided into dozens to hundreds of zones, and the flow information of each zone is obtained through CFD calculation. Subsequently, using the flow information, a kinetic or PBE calculation is implemented in each zone using a numerical solver such as MATLAB. Using the CFD-based compartmental model, the long-term calculation of the kinetics or PBM can be performed in hundreds of zones, whereas it is impossible to simulate millions of computational nodes in only CFD simulations. Bezzo et al. [29] first proposed this approach for modeling a bioreactor; subsequently, the approach was used for an ozone and carbonation process, separately [24,30]. However, it has not been applied to FBRs.

†To whom correspondence should be addressed.
E-mail: jongmin@snu.ac.kr
Copyright by The Korean Institute of Chemical Engineers.

It is difficult to use this approach in FBRs owing to challenges arising from changes in the flow due to particle aggregation and breakage. Moreover, it is inappropriate to use initial flow from CFD in PBM calculation for long-term behaviors because the phenomena render the particles larger or smaller and the varying particle sizes change the flow. To use the CFD-based compartmental model in an FBR, it is essential to update the flow information periodically in a computationally amenable fashion.

In this research, we propose a two-way coupled CFD-DQMOM approach that is similar to the CFD-based compartmental model but updates the flow information periodically from CFD. Subsequently, we applied the approach to a long-term dynamic simulation of an FBR. For verification, the approach was compared to CFD-QMOM, which simulates the flow and QMOM in CFD only. After the verification, a 6 h simulation of the FBR was successfully performed using the proposed approach.

MODELING OF GAS-SOLID FLOW IN FBR

1. Flow Model

The Eulerian-Eulerian approach with the kinetic theory of granular flow was used as a two-phase model. The mass and momentum conservation equations are expressed as follows:

$$\frac{\partial(\alpha_k\rho_k)}{\partial t}+\nabla\cdot(\alpha_k\rho_k\mathbf{u}_k)=0, \tag{1}$$

$$\begin{aligned}\frac{\partial(\alpha_k\rho_k\mathbf{u}_k)}{\partial t}+\nabla\cdot(\alpha_k\rho_k\mathbf{u}_k\mathbf{u}_k)&=-\alpha_k\nabla P-\nabla P_s\\&+\nabla\cdot\tau_k+\alpha_k\rho_k g+K_{gs}(\mathbf{u}_g-\mathbf{u}_s)\end{aligned} \tag{2}$$

where α, ρ, $\mathbf{u}$, and P are the volume fraction, density, velocity, and pressure, respectively, and k denotes each phase. K_{gs} is the drag coefficient between the gas and solid phases, and P_s is the solid pressure when considering particle interaction. No ∇P_s term exists in the gas phase.

$$P_s=\alpha_s\rho_s\theta_s+2\rho_s(1+e_{ss})\alpha_s^2 g_{0,ss}\theta_s, \tag{3}$$

where θ_s, e_{ss}, and $g_{0,ss}$ are the granular temperature, restitution coefficient, and radial distribution function, respectively.

$$g_{0,ss}=\left[1-\left(\frac{\alpha_s}{\alpha_{s,max}}\right)^{\frac{1}{3}}\right]^{-1} \tag{4}$$

The energy balance for the fluctuating kinetic energy is expressed as follows:

$$\begin{aligned}\frac{3}{2}\left[\frac{\partial}{\partial t}(\alpha_s\rho_s\theta_s)+\nabla\cdot(\alpha_s\rho_s\mathbf{u}_s\theta_s)\right]&=(-P_sI+\tau_s):\nabla\mathbf{u}_s\\&+\nabla\cdot(k_{\theta_s}\nabla\theta_s)-\gamma\theta_s+\varphi_{gs}\end{aligned} \tag{5}$$

The diffusion coefficient for granular energy, collisional dissipation of energy, and energy exchange between the gas and solid phases are written as follows:

$$\begin{aligned}k_{\theta_s}=\frac{15d_s\rho_s\alpha_s\sqrt{\pi\theta_s}}{4(41-33\eta)}&\left[1+\frac{12}{5}\eta^2(4-3\eta)\alpha_s g_{0,ss}\right.\\&\left.+\frac{16}{15}(41-33\eta)\eta\alpha_s g_{0,ss}\right]\end{aligned} \tag{6}$$

$$\gamma_{\theta_s}=\frac{12(1-e_{ss}^2)g_{0,ss}}{d_s\sqrt{\pi}}\rho_s\alpha_s^2\theta_s^{\frac{3}{2}} \tag{7}$$

$$\varphi_{gs}=-3K_{gs}\theta_s, \tag{8}$$

where d_s and η are the particle diameter and $(1+e_{ss})/2$, respectively. The phase stress-strain tensors $\nabla\cdot\tau_s$ and $\nabla\cdot\tau_g$ are expressed as

$$\tau_s=\alpha_s\mu_s(\nabla\mathbf{u}_s+\nabla\mathbf{u}_s^T)+\alpha_s\left(\lambda_s-\frac{2}{3}\mu_s\right)\nabla\cdot\mathbf{u}_s \tag{9}$$

$$\tau_g=\alpha_g\mu_g(\nabla\mathbf{u}_g+\nabla\mathbf{u}_g^T)-\frac{2}{3}\alpha_g\mu_g\nabla\cdot\mathbf{u}_g, \tag{10}$$

where μ_s and λ_s are formulated as

$$\begin{aligned}\mu_s&=\mu_{s,col}+\mu_{s,kin}\\&=\frac{4}{5}\alpha_s^2\rho_s d_s g_{0,ss}(1+e_{ss})\sqrt{\frac{\theta}{\pi}}\\&+\frac{5\sqrt{\pi}}{48}\frac{(\rho_s d_s)}{(1+e_{ss})g_{0,ss}}\left(1+\frac{4}{5}(1+e_{ss})\alpha_s\right)^2\sqrt{\theta}\end{aligned} \tag{11}$$

$$\lambda_s=\frac{4}{3}\alpha_s\rho_s d_s g_{0,ss}(1+e_{ss})\sqrt{\frac{\theta}{\pi}} \tag{12}$$

Among the several reported drag models for the gas-solid interphase, the following Gidaspow drag function was employed:

For $\alpha_g\le 0.8$,

$$K_{gs}=150\frac{\alpha_s^2\mu_g}{\alpha_g d_s^2}+1.75\frac{\alpha_s\rho_g}{d_s}|\mathbf{u}_g-\mathbf{u}_s| \tag{13}$$

For $\alpha_g>0.8$,

$$K_{gs}=\frac{3}{4}\frac{C_d(\alpha_s\rho_g)}{d_s}|\mathbf{u}_g-\mathbf{u}_s|\alpha_g^{-2.65} \tag{14}$$

$$C_d=\begin{cases}\frac{24}{Re_s}[1+0.15(Re_s)^{0.687}] & ,\ Re_s<1{,}000\\ 0.44 & ,\ Re_s>1{,}000\end{cases}$$

2. PBM

The PBM based on the number density function (NDF) for a particle in an arbitrary region can be expressed as

$$\begin{aligned}\frac{\partial n(L;\mathbf{x},t)}{\partial t}+\nabla\cdot[\vec{\mathbf{u}}n(L;\mathbf{x},t)]&=B_{ag}(L;\mathbf{x},t)\\&-D_{ag}(L;\mathbf{x},t)+B_{br}(L;\mathbf{x},t)-D_{br}(L;\mathbf{x},t),\end{aligned} \tag{15}$$

where n(L; **x**, t) is the NDF; L is the particle size; **x** is the particle velocity vector; B_{ag}(L; **x**, t) and D_{ag}(L; **x**, t) are the birth and death density functions arising from particle aggregation, respectively; B_{br}(L; **x**, t) and D_{br}(L; **x**, t) are the birth and death density functions due to particle breakage, respectively.

2-1. QMOM

QMOM is a method to solve the PBM using moment equations and quadrature approximation. The moments of the particle size distribution (PSD) are defined as

$$m_i(\mathbf{x},t)=\int_0^\infty n(L;\mathbf{x},t)L^i dL \qquad i=0,1,\cdots,2N-1, \tag{16}$$

where i is the specified number of moments (i^{th} moment). By applying Eq. (16) to Eq. (15), the i^{th} moment can be obtained as follows:

$$\frac{\partial m_i}{\partial t}+\nabla\cdot[\mathbf{u}m_i]=B_{ag,\,i}(L;\,\mathbf{x},\,t)-D_{ag,\,i}(L;\,\mathbf{x},\,t)+B_{br,\,i}(L;\,\mathbf{x},\,t)-D_{br,\,i}(L;\,\mathbf{x},\,t) \tag{17}$$

$$B_{ag,\,i}(L;\,\mathbf{x},\,t)=\frac{1}{2}\int_0^{\infty}\int_0^{\infty}\beta(L,\,\lambda)(L^3+\lambda^3)^{\frac{i}{3}}n(\lambda;\,\mathbf{x},\,t)n(L;\,\mathbf{x},\,t)d\lambda d \tag{18}$$

$$D_{ag,\,i}(L;\,\mathbf{x},\,t)=\int_0^{\infty}\int_0^{\infty}L^i\beta(L,\,\lambda)n(\lambda;\,\mathbf{x},\,t)n(L;\,\mathbf{x},\,t)d\lambda dL \tag{19}$$

$$B_{br,\,i}(L;\,\mathbf{x},\,t)=\int_0^{\infty}\int_0^{\infty}L^i a(\lambda)b(L|\lambda)n(\lambda;\,\mathbf{x},\,t)d\lambda dL \tag{20}$$

$$D_{br,\,i}(L;\,\mathbf{x},\,t)=\int_0^{\infty}\int_0^{\infty}L^i a(L)n(L;\,\mathbf{x},\,t)dL, \tag{21}$$

where $\beta(L,\lambda)$ is the aggregation kernel of two particles with lengths L and λ, separately. $\alpha(\lambda)$ is the breakage kernel of length λ, and $b(L/\lambda)$ is the probability distribution of length L's breakage, which contains the information of fragment particles produced when particle breakage occurs. A moment can be calculated by the following quadrature approximation:

$$m_i(\mathbf{x},\,t)=\int_0^{\infty}n(L;\,\mathbf{x},\,t)L^i dL\approx\Sigma_{p=1}^{N}w_{s_p}L_{s_p}^i \qquad i=0,\,1,\,\cdots,\,2N-1, \tag{22}$$

where s_p is the phase of particle p. Applying Eq. (22) to Eq. (17) yields the following quadrature form of moments:

$$\frac{\partial m_i}{\partial t}+\nabla\cdot[\mathbf{u}m_i]=\frac{1}{2}\sum_p^N w_{s_p}\sum_q^N w_{s_q}(L_{s_p}^3+L_{s_q}^3)^{\frac{i}{3}}\beta(L_{s_p},\,L_{s_q})-\Sigma_p^N L_{s_p}^i w_{s_p}\Sigma_q^N w_{s_q}\beta(L_{s_p},\,L_{s_q})+\Sigma_p^N a_{s_p}\overline{b_{s_p}^i}w_{s_p}-\Sigma_p^N L_{s_p}^i w_{s_p}a(L_{s_p}) \tag{23}$$

The following aggregation and breakage functions were used, which are widely used in the polymerization process [31,32]:

$$\beta(L_{s_p},\,L_{s_q})=c_{aggre}(L_{s_p}^2+L_{s_q}^2)/(L_{s_p}L_{s_q})^4 \tag{24}$$

$$a(L_{s_p})=c_{break}L_{s_p}^2, \tag{25}$$

where c_{aggre} and c_{break} are the aggregation and breakage kernel constants, respectively. Because the objective of this study is to show the advantage of the proposed model by showing the reliable results and comparing it with the conventional model, we adopted general kernel functions and constants used in a similar FBR process. The probability distribution function is described based on a uniform breakage mechanism expressed as follows:

$$b(L_{s_p}|L_{s_q})=\frac{6L_{s_p}^2}{L_{s_q}^3} \qquad \text{if } 0<L_{s_p}<L_{s_q}\ (\text{else}=0) \tag{26}$$

$$\overline{b_p^i}=2^{\frac{3-i}{3}}L_{s_p}^i \tag{27}$$

By solving Eq. (23), the moments of the PSD can be tracked; subsequently, w_{s_p} and L_{s_p} can be obtained using the product-difference algorithm [33].

The limitation of the QMOM is that each particle phase cannot be computed separately. So, if CFD and QMOM are combined, the drag coefficients from light to heavy particles cannot have distinct values; therefore, the same particle profile will be shown for each particle. Solving Eq. (23) allows only the moments of all the particles to be tracked; w_{s_p} and L_{s_p} are derived through the moments of all the particles.

2-2. DQMOM

In the DQMOM, n(L; **x**, t) is approximated as an impulse train comprising N Dirac delta functions as follows:

$$n(L;\,\mathbf{x},\,t)\approx\Sigma_{p=1}^{N}w_{s_p}(\mathbf{x},\,t)\delta[L-L_{s_p}(\mathbf{x},\,t)] \tag{28}$$

Substituting Eq. (15) into (28) yields the following approximate PBM equation:

$$\begin{aligned}&\Sigma_{p=1}^{N}\delta(L-L_{s_p})\left[\frac{\partial w_{s_p}}{\partial t}+\nabla\cdot(w_{s_p}u_{s_p})\right]\\&-\Sigma_{p=1}^{N}\delta'(L-L_{s_p})\left[w_{s_p}\left(\frac{\partial L_{s_p}}{\partial t}+u_{s_p}\nabla L_{s_p}\right)\right]\\&=B_{ag}(L;\,\mathbf{x},\,t)-D_{ag}(L;\,\mathbf{x},\,t)+B_{br}(L;\,\mathbf{x},\,t)\\&-D_{br}(L;\,\mathbf{x},\,t)=S(L,\,L_{s_p};\,\mathbf{x},\,t),\end{aligned} \tag{29}$$

where $\delta'(L-L_{s_p})$ is the first time derivative of $\delta(L-L_{s_p})$, and the breakage and aggregation kernels are the same as those of the QMOM. By substituting Eqs. (30) and (31) into Eq. (29), Eq. (32) can be derived as follows:

$$\frac{\partial w_{s_p}}{\partial t}+\nabla\cdot(w_{s_p}u_{s_p})=a_{s_p} \tag{30}$$

$$\frac{\partial w_{s_p}L_{s_p}}{\partial t}+\nabla\cdot(w_{s_p}L_{s_p}u_{s_p})=b_{s_p} \tag{31}$$

$$\Sigma_{p=1}^{N}\delta(L-L_{s_p})a_{s_p}-\Sigma_{p=1}^{N}\delta'(L-L_{s_p})[b_{s_p}-L_{s_p}q_{s_p}]=S(L,\,u_{s_p};\,\mathbf{x},\,t) \tag{32}$$

Combining Eq. (22) and (32) yields

$$\Sigma_{p=1}^{N}a_{s_p}L_{s_p}^i(1-i)+ib_{s_p}L_{s_p}^{i-1}=\overline{S_i}, \tag{33}$$

where

$$\overline{S_i}=\int_0^{\infty}S(L)L^i dL=B_{ag,\,i}(L;\,\mathbf{x},\,t)-D_{ag,\,i}(L;\,\mathbf{x},\,t)+B_{br,\,i}(L;\,\mathbf{x},\,t)-D_{br,\,i}(L;\,\mathbf{x},\,t) \tag{34}$$

a_{s_p} and b_{s_p} are calculated through a linear system of the first 2N moments of the PSD. The linear system is written in the matrix form as follows:

$$Ay=z, \tag{35}$$

where the 2N×2N matrix A is defined as

$$A=\begin{bmatrix}1 & \cdots & 1 & 0 & \cdots & 0\\0 & \cdots & 0 & 1 & \cdots & 1\\-L_{S_1}^2 & \cdots & -L_{S_N}^2 & 2L_{S_1} & \cdots & 2L_{S_N}\\\vdots & \ddots & \vdots & \vdots & \ddots & \vdots\\2(1-N)L_{S_1}^{2N-1} & \cdots & 2(1-N)L_{S_N}^{2N-1} & (2N-1)L_{S_1}^{2N-2} & \cdots & (2N-1)L_{S_N}^{2N-2}\end{bmatrix} \tag{36}$$

The 2N vectors of x and d are expressed as

$$y=[a_{S_1}\cdots a_{S_N}\,b_{S_1}\cdots b_{S_N}]^T \tag{37}$$

$$z=[S_0\cdots S_{2N-1}]^T \tag{38}$$

If is L_{s_p} unique, then A will have a full rank and be invertible. In this

case, L_{s_p} and w_{s_p} can be obtained easily by inverting A as follows:

$$y = A^{-1}z \tag{40}$$

$$\begin{pmatrix} a_{S_1} \\ \vdots \\ a_{S_N} \\ b_{S_1} \\ \vdots \\ b_{S_N} \end{pmatrix} = \begin{bmatrix} 1 & \cdots & 1 & 0 & \cdots & 0 \\ 0 & \cdots & 0 & 1 & \cdots & 1 \\ -L_{S_1}^2 & \cdots & -L_{S_N}^2 & 2L_{S_1} & \cdots & 2L_{S_N} \\ \vdots & \ddots & \vdots & \vdots & \ddots & \vdots \\ 2(1-N)L_{S_1}^{2N-1} & \cdots & 2(1-N)L_{S_N}^{2N-1} & (2N-1)L_{S_1}^{2N-2} & \cdots & (2N-1)L_{S_N}^{2N-2} \end{bmatrix}^{-1} \begin{pmatrix} \overline{S_0} \\ \vdots \\ \overline{S_{2N-1}} \end{pmatrix} \tag{41}$$

The advantage of the DQMOM is that it can obtain each particle distribution separately with distinct drag coefficients and provide reasonable predictions with N=3 for monovariate system [34, 35]. However, a large computational load caused by simulating all the particle phases and the numerical problem associated with inverting a high-dimensional matrix requires a short time step: 10^{-7} to 10^{-9} s. This is the main reason we used CFD-QMOM, despite its limitations, instead of CFD-DQMOM to verify the two-way coupled CFD-DQMOM approach [36].

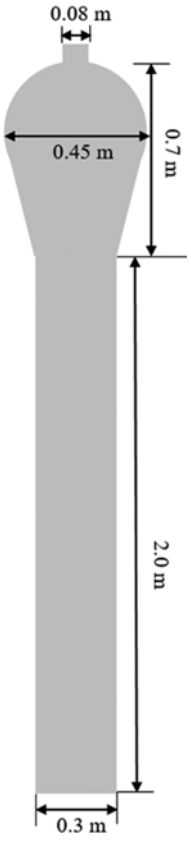

Fig. 1. FBR configuration.

REACTOR GEOMETRY AND CONDITIONS

As shown in Fig. 1, the height of the FBR was 2.7 m. The diameter was 0.3 m at the bottom of the reactor, which was increased to 0.45 m and then decreased again. This type of reactor is widely used to produce dynamic flow that can mix the particles well [37].

The particles were initially packed from the bottom to 1 m and had three particle sizes: 100 (s_1), 300 (s_2), and 700 μm (s_3). The s_1, s_2, and s_3 had initial volume fractions of 0.18, 0.3, and 0.12, respectively. The solid density was 980 kg/m^3 and a superficial air velocity of 0.3 m/s was introduced at the bottom of the FBR. The operating temperature and pressure were 70 °C and 22 bar, respectively, which are general operating conditions of a linear low-density polyethylene process [37].

The aggregation and breakage kernel constants, c_{aggre} and c_{break}, were 1e-35 and 5e-4, respectively. These values are very large (100 times larger than the general constants). Such large values were used to compare the two-way coupled CFD-DQMOM with CFD-QMOM, which requires a long time to simulate flow and QMOM simultaneously in CFD. However, a simulation time of several hours does not require a long time in the two-way coupled CFD-DQMOM. Because a simulation time longer than several minutes cannot be performed in CFD-QMOM, we increased the kernel constants and compared the two models for 60 s.

TWO-WAY COUPLED CFD-DQMOM

1. Extraction of Flow Information from CFD

To extract flow information from the CFD, the reactor was divided in both vertical and horizontal directions. Four zones were created on each floor and the number of floors was determined by the sensitivity analysis described in Section 5.1.3. Subsequently, from the CFD-hydrodynamics model, $\alpha_{s_p}^{(i,j)}$, the volume fraction of particle p in the i^{th} floor of the j^{th} zone was obtained and used as an initial condition of the DQMOM equations (See Fig. 2).

2. Two-way Coupled CFD-DQMOM Simulation

For the two-way coupled CFD-DQMOM simulation, the CFD-hydrodynamics simulation, which calculates only flow without the PBM in CFD, proceeds until the flow are relatively stable. It was con-

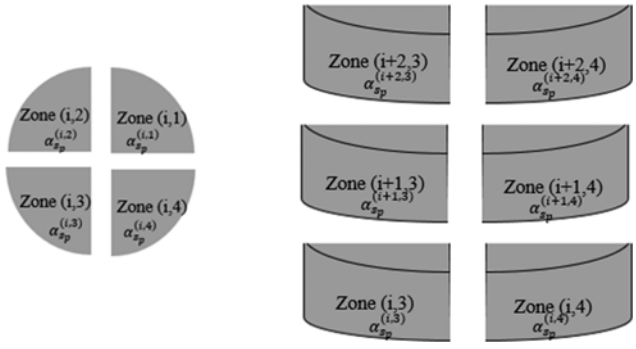

Fig. 2. Zone configuration and particle volume fraction ($\alpha_{s_p}^{(i,j)}$).

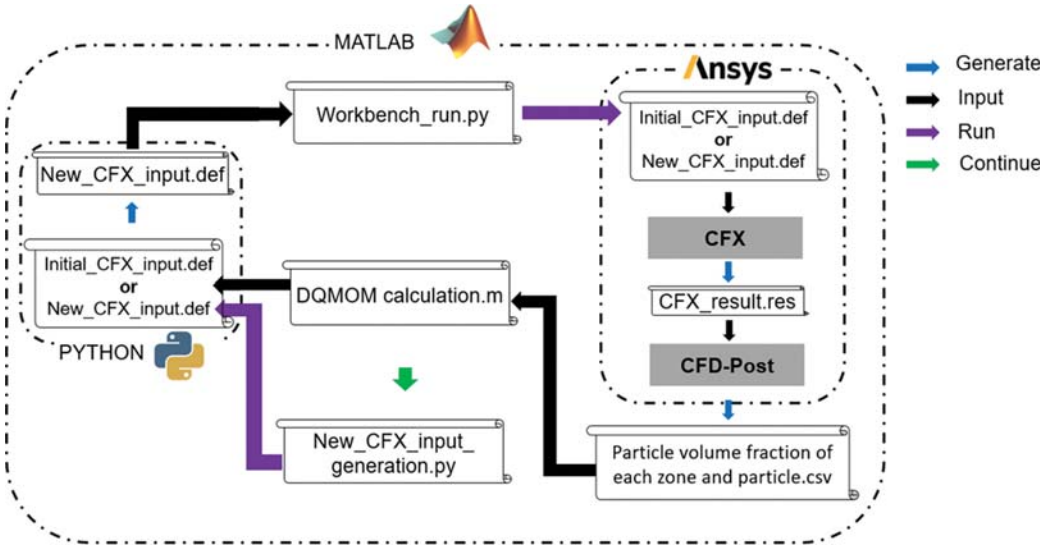

Fig. 3. Systematic diagram for two-way coupled CFD-DQMOM simulation.

firmed that a simulation time of approximately 15 s was sufficient to acquire nearly steady-state flow. From the simulation, the particle volume fraction of each zone and particle was obtained. Using the data above, the DQMOM equations (Eqs. (30)-(41)) were solved for each zone in MATLAB, where the convection of particles between the zones in Eqs. (31) and (31) was assumed to be zero because the changes in the flow were negligible after 15 s. To reflect the DQMOM results and update the flow in the FBR, a CFD setup was established for the particle length and particle volume fraction of each zone. Additionally, each particle was modified and the CFD simulation was implemented again to obtain the updated flow (See Fig. 3).

A sensitivity analysis was performed to determine the time interval required to update the flow information. Based on the analysis, 10 s was selected with slight changes in the results when the time interval was further decreased (see Supplementary Material for details). We used a large aggregation and breakage kernel to compare the results with the CFD-QMOM results, where the large kernels resulted in a sudden change in the flow over several seconds, requiring a short time interval. However, when the constants of the kernels were not large, a time interval of 15 min or 1 h was appropriate for updating the flow information.

SIMULATION SETUP

CFD packages of ANSYS CFX 19.5 and FLUENT 18.2 (Ansys, USA) were used for CFD simulations. The reactor geometry and meshes were generated using the DesignModular and AnsysMeshing modules, respectively, and simulations were performed on an Intel Xeon E5-2690 (24 cores) with 128 GB RAM. The number of nodes was determined to be 307,776 based on the mesh robustness test (see Supplementary Material for details).

A standard k-ε model was used as a turbulence model. For the inlet condition, a uniform inlet condition was specified at the bottom of the reactor. The outlet condition was set as the gauge static pressure of 0 Pa. At the walls, no-slip conditions were applied for both the gas and solid phases.

1. Two-way Coupled CFD-DQMOM

1-1. CFD-hydrodynamic Simulation

An upwind was selected for the advection scheme, and the first-order backward Euler was used for the transient scheme. The convergence loops were within 1-20, and the convergence criterion of 10^{-4} with a time step of 0.002-0.005 s was set. The particle volume fraction and the lengths of each zone and each particle calculated from the DQMOM in MATLAB were set as the initial conditions for the next step using a user-defined function.

1-2. DQMOM Simulation in MATLAB

To solve the DQMOM equations, particle length normalization was first performed; we used 1, 3, and 7 instead of 100, 300, and 700 μm as the particle lengths for stability [38]. The timestep was set to 0.001 s, and we confirmed that a further decrease in the time step did not change the DQMOM calculation results. The DQMOM calculation was continued using Eqs. (30)-(41), and the final solutions of the DQMOM, the particle volume fraction, and the lengths

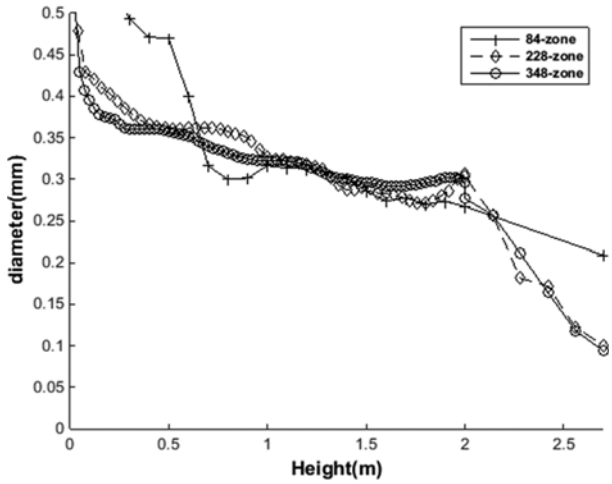

Fig. 4. d_{32} along the height for the 84-, 228-, and 348-zone models.

of each zone and each particle were applied as the initial conditions for the next CFD-hydrodynamics model.

1-3. Zoning Method

Sensitivity analysis was employed to determine the appropriate number of floors in the FBR. We increased the number of floors from 21 (84-zone) to 87 (348-zone), and the sensitivity analysis confirmed that 57 floors (228-zone) were appropriate based on changes in the computational results, which were negligible with a further increase in the number of floors (See Fig. 4 and Supplementary Material for the details).

2. CFD-QMOM Simulation Setup

The CFD-QMOM simulation was performed using FLUENT's built-in QMOM module. Furthermore, FLUENT's built-in DQMOM module was available; however, it requires an excessive amount of computational resources, e.g., a time step of 10^{-7} s, rendering it infeasible to simulate for 60 s, and some stability issues have been reported. Moreover, we encountered a stability issue when using FLUENT's own DQMOM code [39]. In the QMOM simulation, we set the minimum and maximum sizes of the particles to 0.08 and 2 mm, respectively. The volumetric shape factor (k_v) was set to $\pi/6$ and the total number of moments was six. A phase-coupled SIMPLE scheme was set and the first-order upwind scheme was used. The convergence loops were within 1-40 and a fixed time step of 0.001 s was set.

RESULTS AND DISCUSSION

Because no experimental results existed, we verified the two-way coupled CFD-DQMOM model through the appropriateness of the simulation results and comparison with the CFD-QMOM model. In Section 6.1, it was first confirmed that the model can show reasonable results by analyzing several particle variables. After that, the model was compared to the CFD-QMOM for 60 s with large aggregation and breakage constants in Section 6.2. In Section 6.3, using normal aggregation and breakage constants, a simulation was performed for 6 h using the model.

1. Two-way Coupled CFD-DQMOM Results

For the 60 s FBR simulation, a CFD simulation without DQMOM calculation was first performed. In the first CFD-hydrodynamics calculation, each particle had a constant particle size and the flow was primarily affected by the drag force calculated from the constant particle size. Because the particle aggregation effect was not considered in the CFD hydrodynamics, the particles could rise higher in the FBR. Hence, using the Gidaspow drag model without any correction for the drag effect caused the solid bed height to be larger; several drag models including the energy minimization multi-scale drag model, which introduces the drag force correction factor to account for particle aggregation and breakage, have been studied for the validation of solid bed height [40-42]. After the CFD-hydrodynamics calculation, the particle volume fractions and lengths of each zone were sent to MATLAB for the DQMOM calculation. In the latter, the particle volume fractions and lengths of each zone were obtained and sent to the CFD-hydrodynamics model again to update the flow information. As shown in Fig. 5, the flow of the second CFD-hydrodynamics model differed from that of the first one. The main difference was the light particle (s_1), which was clustered and whose diameter was larger than the original particle size. Consequently, at the top part of the FBR, the clustering effect was reflected through the DQMOM calculation and the solid bed height was reduced. In Fig. 5, it is shown that the final flow (rightmost figure) differed significantly from the initial flow (leftmost figure); the initial flow is steady-state flow with-

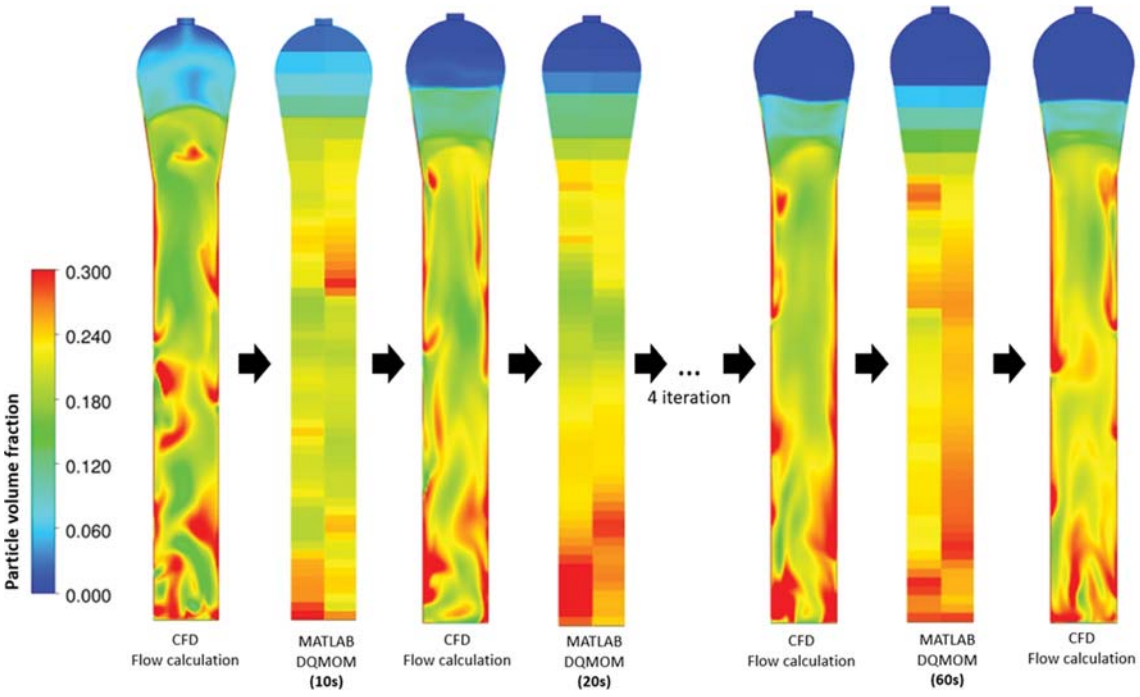

Fig. 5. Particle volume fraction profiles for 60 s in the two-way coupled CFD-DQMOM model.

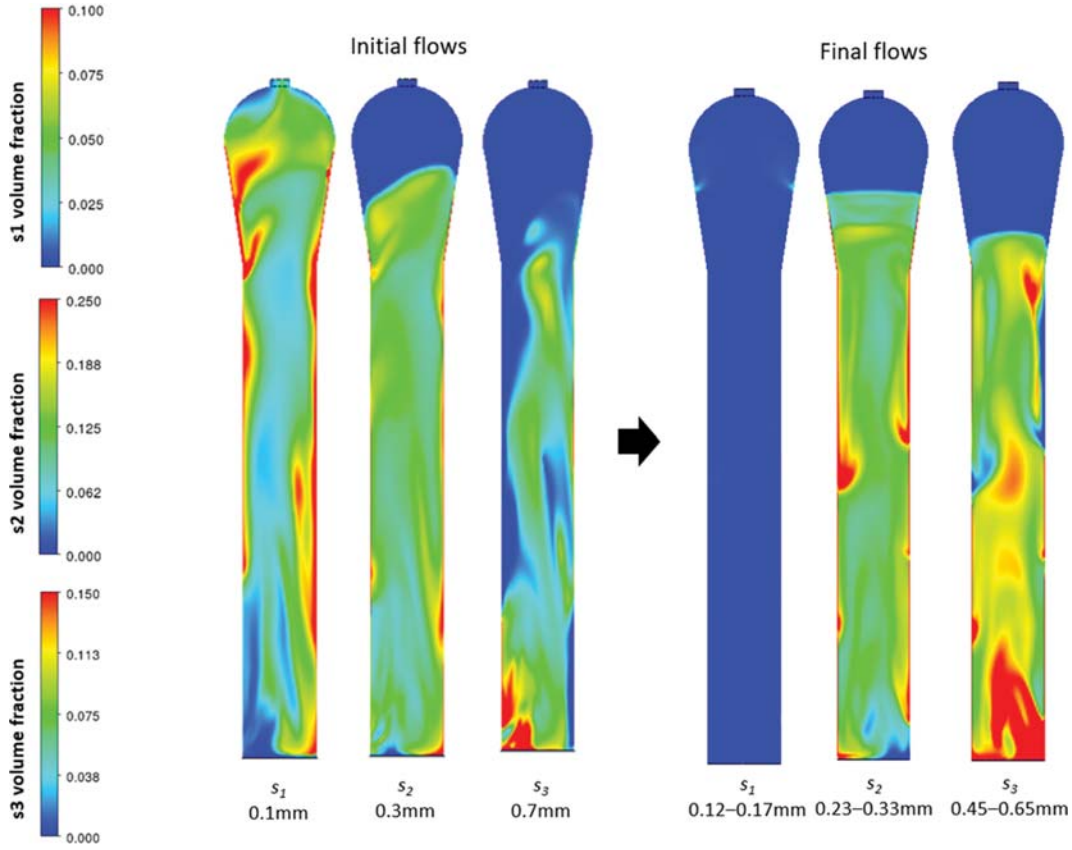

Fig. 6. Particle volume fraction profiles for each particle at the initial and final states.

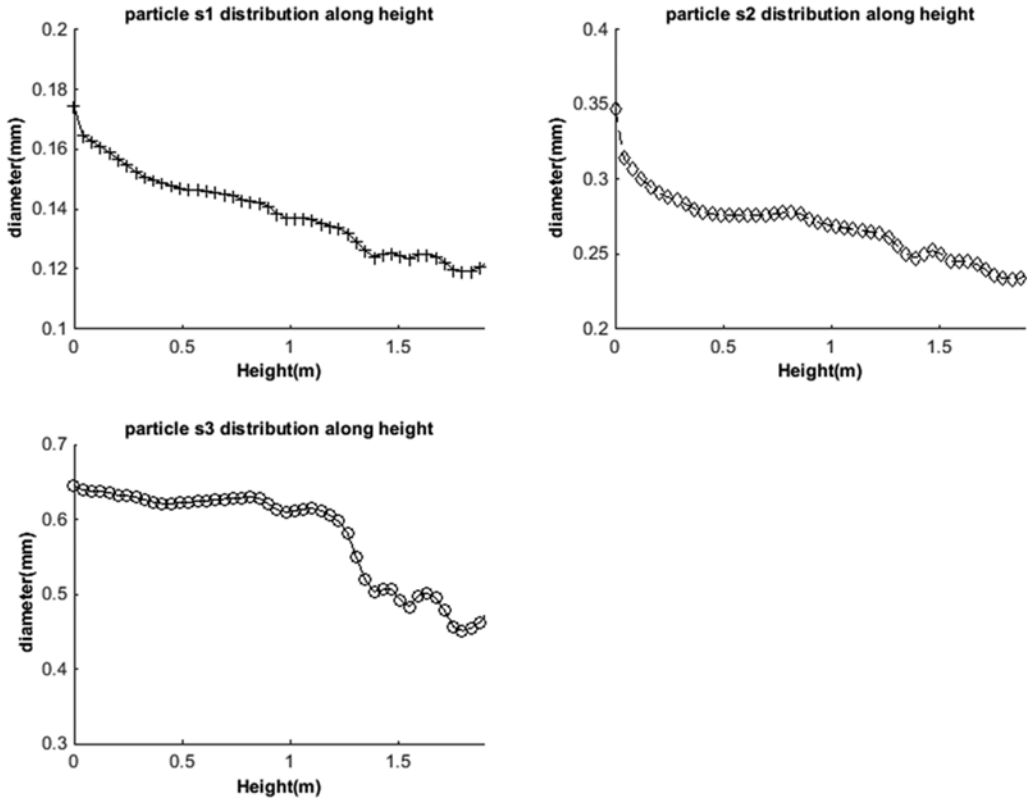

Fig. 7. d_{32} along the height for s_1, s_2, and s_3 particles.

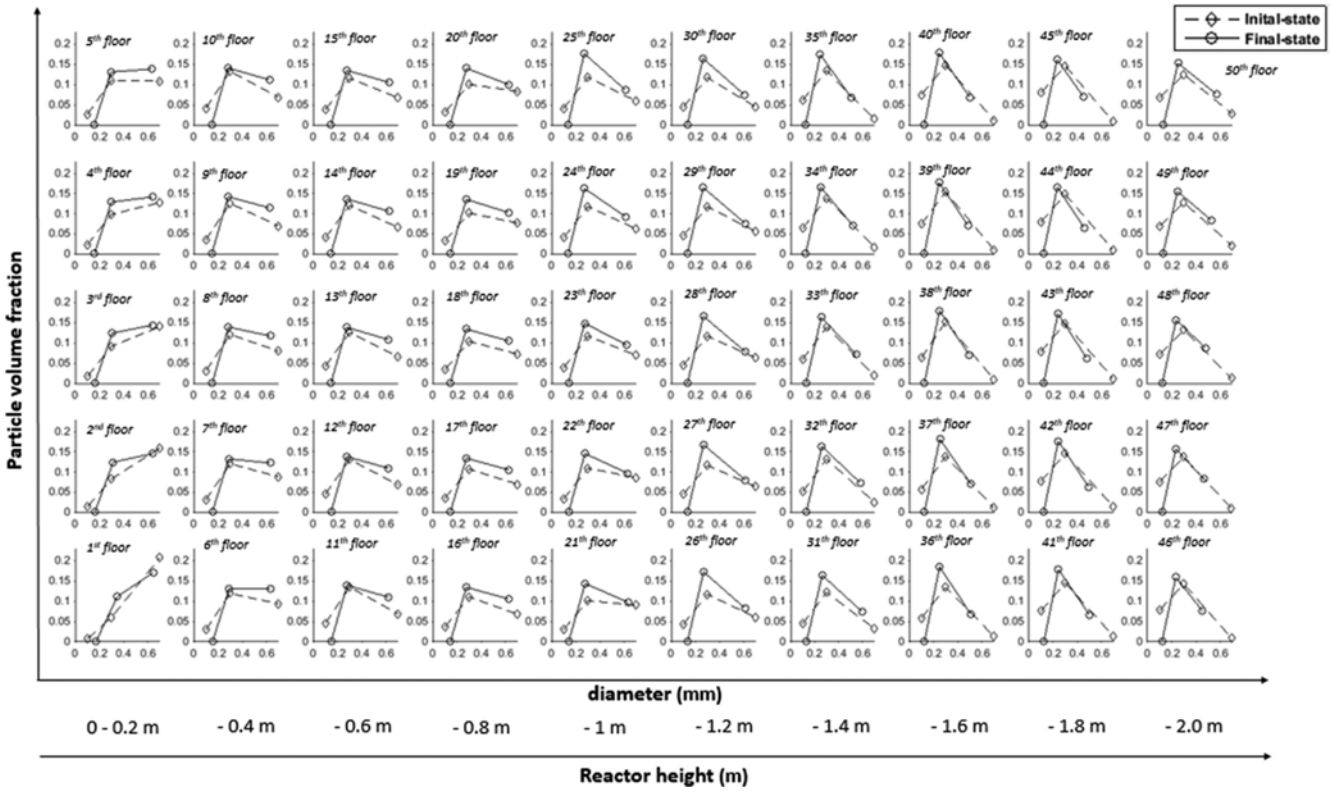

Fig. 8. Particle size distribution from the 1st to 50th floor in the initial and final states.

out calculation of DQMOM and the final flow is the result after 60 s of calculation of DQMOM. Detailed analysis on the initial and final flows is shown in Fig. 6. The representative diameter of s_1 particles increased from 0.1 mm to 0.12-0.17 mm and most of the s_1 particles grew to the size of s_2 particles, with a low s_1 particle volume fraction left at the final flow. Meanwhile, the representative diameter of s_3 particles decreased from 0.7 to 0.45-0.65 mm and some of the s_2 particles grew to the size of the s_3 particles, causing an increase in the total volume fraction of the s_3 particles. The s_2 particles showed a similar volume fraction profile, as shown in Fig. 6; however, the d_{32} distribution along the height indicated a decreasing d_{32} along the height (see Fig. 7), which could not be modeled in the CFD-hydrodynamics model with a constant particle size in all parts of the FBR. On the other hand, there was the entrainment of 0.6 kg of s_1 particle from the initial to final flows for 60 s. As shown in Figs. 5 and 6, final flows which considered particle interactions have few entrainments. If particle interactions were considered in CFD from the beginning, entrainment would not have occurred, but in this model, since final flows were obtained from several CFD-hydrodynamics model including initial flows, there was an error arising from the entrainment. However, the entrainment of 0.6 kg of s_1 particle accounts for only about 1.6% of particles, which is an acceptable error.

The particle size distributions at each floor are shown in Fig. 8. At the bottom part (0-0.2 m), the s_3 particles dominated from the initial to the final state. This is a predicted result that a heavy particle exists at the bottom. As the height of the FBR increased, the ratio of particle s_2 increased, whereas that of s_3 decreased and the sum of all the particle volume fractions decreased. In the final state, particle s_1 rarely appeared and the volume fraction of particles s_2 and s_3 increased compared with the initial state. The representative diameter of s_3 decreased and the diameter of s_1 increased in all

Table 1. Mean diameter and ratio of each particle for the CFD-hydrodynamics, two-way coupled CFD-DQMOM, and CFD-QMOM models

Model	CFD-hydrodynamics	Two-way CFD-DQMOM	CFD-QMOM
s_1 Mean diameter (mm)	0.1	0.140	0.154
s_2 Mean diameter (mm)	0.3	0.265	0.260
s_3 Mean diameter (mm)	0.7	0.590	0.588
s_1 Particle ratio	0.3	0.0004	0.0577
s_2 Particle ratio	0.5	0.6425	0.7571
s_3 Particle ratio	0.2	0.3571	0.1852

parts. The representative diameter of s_2 increased at the bottom part (0-0.2 m) but decreased in the other parts.

These results confirmed that the CFD-hydrodynamics model, a traditional CFD model, cannot yield reliable results owing to challenges in considering particle interactions. Previous studies have reported that the conventional CFD model cannot be validated without any special tuning for the drag function [43-45]. The two-way coupled CFD-DQMOM model can visualize realistic flows, including several particle interactions.

2. CFD-QMOM Results

To verify the two-way coupled CFD-DQMOM approach, CFD-QMOM calculation was performed for 60 s through FLUENT's QMOM implementation code. Table 1 shows the mean diameter and ratios of each particle at 60 s. All the particles' mean diameters of the CFD-QMOM model converged to those of the two-way coupled CFD-DQMOM model with little error; only the mean diameter of particle s_1 indicated an error of approximately 10%. Meanwhile, the ratio of particle s_1 decreased significantly, whereas that of s_2 increased in the two models. The ratio of particle s_3 increased in the two-way coupled CFD-DQMOM model but decreased in the CFD-QMOM model. All the errors in the particle ratio and s_1 mean diameter were caused by the limitations of the CFD-QMOM model. This was because the Eulerian-Eulerian approach of the CFD-QMOM model only considered the gas and solid phases without a distinct particle phase, i.e., a two-phase model. As shown in Fig. 9 (right), in the CFD-QMOM model, the particle volume fraction profiles of all the particles were the same except for the absolute value. Consequently, a light particle could not float higher and a heavier particle could not settle down. Because the s_1 particles could not float higher, they appeared throughout the reactor and had a larger s_1 volume fraction than the two-way coupled CFD-DQMOM model. In addition, because the s_3 particles could not settle down, they had a much smaller volume fraction than the two-way coupled CFD-DQMOM model. As shown in Figs. 8 and 9, at the bottom part, the s_3 particle volume fraction was approximately 0.15 in the two-way coupled CFD-DQMOM model, whereas the value was approximately 0.04 in the CFD-QMOM model. In addition, the solid bed height was 0.3 m higher in the CFD-QMOM model than the two-way coupled CFD-DQMOM model.

By comparing the two models, a general trend can be predicted for the final mean diameter of each particle; however, the solid volume fraction profile of the two-way coupled CFD-DQMOM model cannot be validated. It is concluded that the two-way coupled CFD-DQMOM model yields more realistic results and requires a shorter time to simulate the reactor. In conclusion, although the two-way coupled CFD-DQMOM model is not fully validated, the proposed scheme can simulate realistic trends and results in a

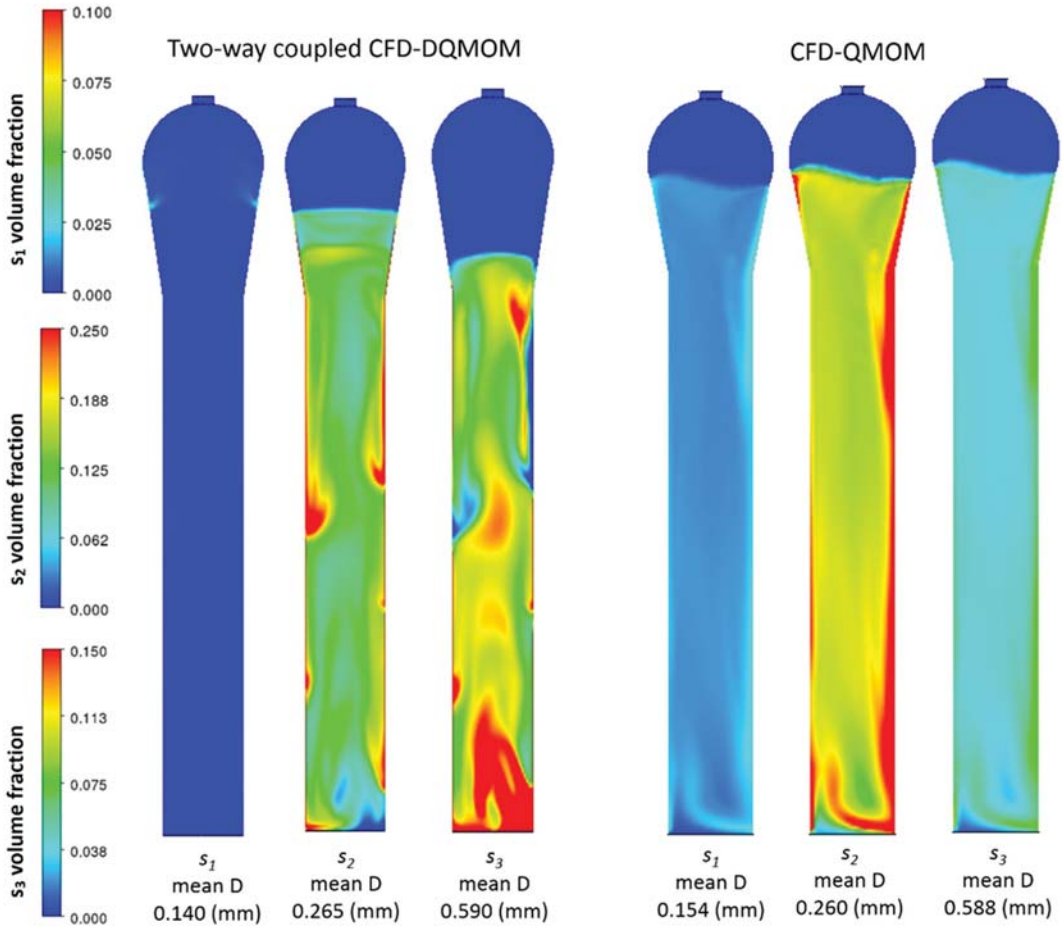

Fig. 9. Particle volume fraction profiles of each particle for two-way coupled CFD-DQMOM model (left) and CFD-QMOM model (right).

much lower computational cost than the CFD-QMOM model.

3. Two-way Coupled CFD-DQMOM for Long-term Simulation

This section describes the capability of the proposed approach in performing long-term simulations. To illustrate, a 6 h simulation was performed using normal kernel constants; the aggregation and breakage kernel constants were 3.33e-38 and 1.67e-6, respectively. The time interval for the flow update was set to 0.5 h. Thus, the flow derived from the CFD-hydrodynamics model was used for the DQMOM calculation in MATLAB for 0.5 h; subsequently, the new CFD-hydrodynamics simulation was performed for updat-

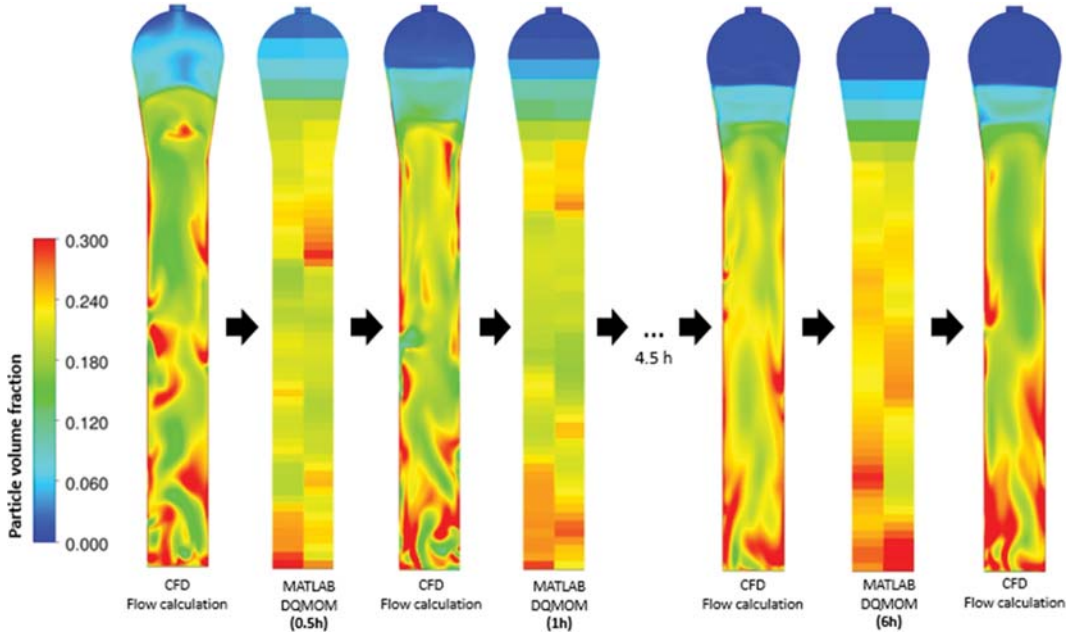

Fig. 10. Particle volume fraction profiles for 6 h in two-way coupled CFD-DQMOM model.

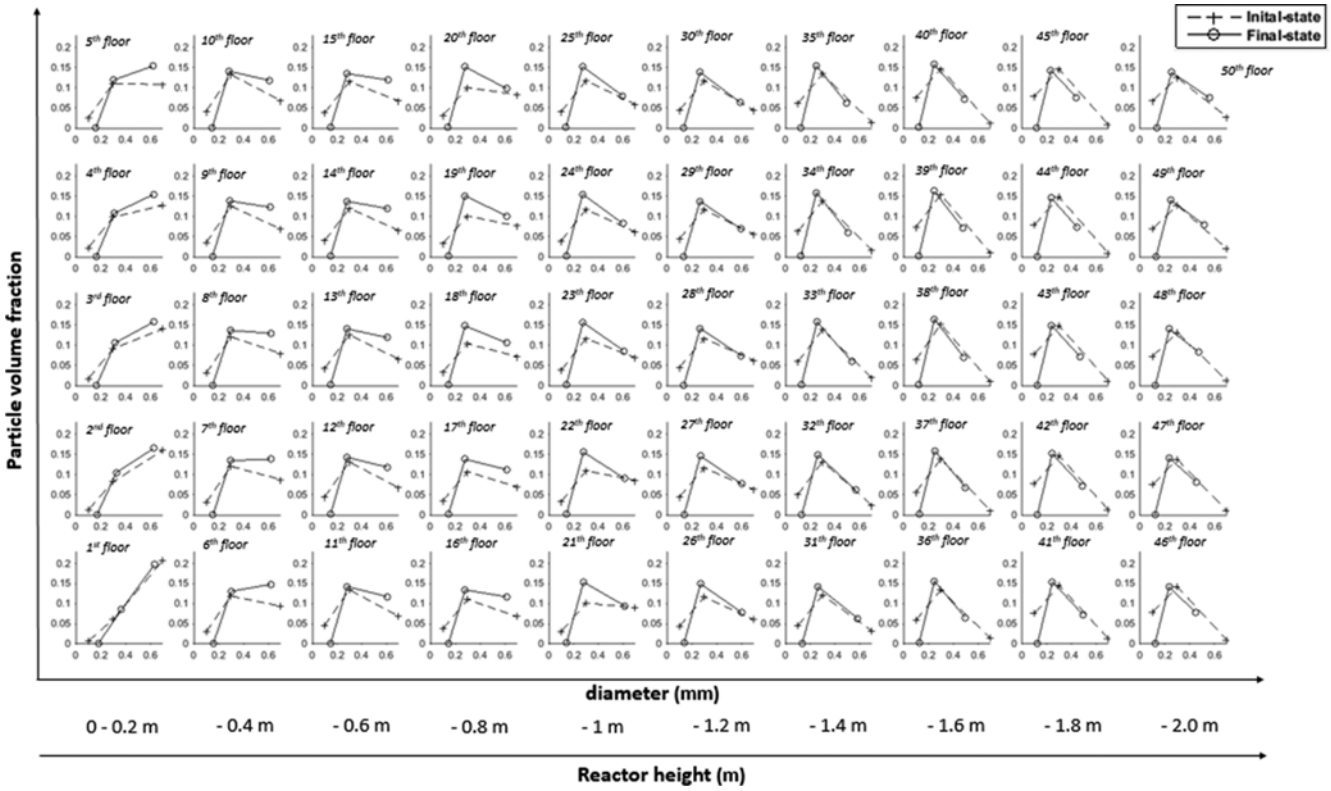

Fig. 11. Particle size distribution from 1st to 50th floor in initial and final states for 6 h simulation.

ing the flow. Because the kernel constants were 300-times smaller, the flow did not change significantly for 0.5 h. It was confirmed that an updating interval of 10 s was appropriate for 300X larger constants in Section 4.2. With linear scaling, an interval shorter than 3,000 s was appropriate for 300X smaller constants. Finally, through 12 updates, a 6 h simulation was completed successfully without any computational problems. As shown in Fig. 10, the solid bed height decreased over time, and Fig. 11 shows changes in the particle size distribution in each floor, which is similar to the results in Section 6.1. Hence, it is concluded that the proposed model can provide the long-term dynamic behavior of FBRs in a reasonable time.

CONCLUSIONS

Owing to exorbitant computation costs, the long-term simulation of FBRs has not been conducted. Hence, most studies reported only instantaneous dynamic behaviors of FBRs accompanied with drag coefficient tuning for validation. This study proposed a two-way coupled CFD-DQMOM approach that enables a long-term dynamic simulation.

The efficacy of the proposed scheme was verified by comparing it with the CFD-QMOM model. The two models indicated similar results, which could not be simulated using conventional CFD; however, an error due to the limitations of the CFD-QMOM model appeared. The CFD-QMOM can calculate only the average particle flows without simulating each of the particle's profiles. While the conventional CFD model with a drag coefficient derived from a constant particle size without considering underlying physical phenomena cannot calculate a realistic particle size distribution, the proposed approach can compute several hydrodynamics, including the growth of light particles, breakage of heavy particles, flow changes, and particle size distribution. Another advantage of the proposed scheme is that long-term dynamic simulations can be performed.

The proposed approach may be useful for simulating chemical reactors involving complex hydrodynamics or multiple phases, such as crystallization, slurries, and fermentation. Furthermore, additional chemical reactions or physical phenomena can be included with only a small supplement of computational load because reaction kinetics and physical phenomena are calculated in hundreds of zones instead of millions of meshes. However, when the chemical reaction or physical phenomena are rapid, the time interval for updating the flow information should be reduced, which may be prohibitive for computational loads for long-term simulations.

ACKNOWLEDGEMENTS

This work was supported by the National Research Foundation of Korea (NRF) grant funded by the Ministry of Science and ICT (MSIT) of the Korean government (No. 2020R1A2C100550311).

NOMENCLATURE

d_s : particle size [m]
d_{32} : sauter mean diameter [mm]
g : gravitational acceleration [m/s^2]
K_{gs} : gas/solid drag coefficient
L : particle size as internal coordinate [m]
m : moments
n : bubble number density
P : pressure [N/m^2]
s_p : phase p among particles
t : time [s]
u : velocity vector [m/s]
w : quadrature weight

Greek Letters

α : phase volume fraction
δ : dirac delta function
μ : molecular dynamic viscosity [Pa s]
λ_s : solid bulk viscosity [Pa s]
ρ : density [kg/m^3]
θ_s : granular temperature [m^2/s^2]
k_{θ_s} : granular energy
γ_{θ_s} : collisional dissipation of energy
φ_{gs} : energy exchange between gas and solid
e_{ss} : restitution coefficient
$g_{0,ss}$: radial distribution function
τ : stress-strain tensor [Pa]

Abbreviations

CFD : computational fluid dynamics
CFD-hydrodynamics model : simulate only hydrodynamics without reactions or the PBM
CFD-QMOM : simulate flows and PBM together in FLUENT's own implementation code
FBR : fluidized bed reactor
PBM : population balance model
QMOM : quadrature method of moments
DQMOM : direct quadrature method of moments
NDF : number density function

Subscripts

g : gas
s : solid
i : specified number of moments

SUPPORTING INFORMATION

Additional information as noted in the text. This information is available via the Internet at http://www.springer.com/chemistry/journal/11814.

REFERENCES

1. C. Kiparissides, *J. Process Control*, **16**, 205 (2006).
2. W. C. Yan, Z. H. Luo, Y. H. Lu and X. D. Chen, *AIChE J.*, **58**, 1717 (2012).
3. Y. Che, Z. Tian, Z. Liu, R. Zhang, Y. Gao, E. Zou, S. Wang and B. Liu, *Powder Technol.*, **286**, 107 (2015).
4. A. D. Randolph and M. A. Larson, *Theory of particulate processes:*

Analysis and techniques of continuous crystallization, Academic Press Inc., New York (1971).
5. J. R. Grace and F. Taghipour, *Powder Technol.*, **139**, 99 (2004).
6. J.-P. Torré, D. F. Fletcher, T. Lasuye and C. Xuereb, *Chem. Eng. Sci.*, **62**, 6246 (2007).
7. J. Jung and I. K. Gamwo, *Powder Technol.*, **183**, 401 (2008).
8. J. A. Mendoza and S. Hwang, *Korean J. Chem. Eng.*, **35**, 11 (2018).
9. F. Kerdouss, A. Bannari and P. Proulx, *Chem. Eng. Sci.*, **61**, 3313 (2006).
10. S. Park, J. Na, M. Kim, J. An, C. Lee and C. Han, *Korean Chem. Eng. Res.*, **54**, 612 (2016).
11. N. Jurtz, M. Kraume and G. D. Wehinger, *Rev. Chem. Eng.*, **35**, 139 (2019).
12. M. Kim, J. Na, S. Park, J.-H. Park and C. Han, *Chem. Eng. Sci.*, **177**, 301 (2018).
13. S. Zimmermann and F. Taghipour, *Ind. Eng. Chem. Res.*, **44**, 9818 (2005).
14. S. Park, J. Na, M. Kim and J. M. Lee, *Comput. Chem. Eng.*, **119**, 25 (2018).
15. R. Fan, D. L. Marchisio and R. O. Fox, *Powder Technol.*, **139**, 7 (2004).
16. S.-S. Liu and W.-D. Xiao, *Chem. Eng. Sci.*, **111**, 112 (2014).
17. Y. Yao, Y.-J. He, Z.-H. Luo and L. Shi, *Adv. Powder Technol.*, **25**, 1474 (2014).
18. Y. Yao, J.-W. Su and Z.-H. Luo, *Powder Technol.*, **272**, 142 (2015).
19. V. Alopaeus, M. Laakkonen and J. Aittamaa, *Chem. Eng. Sci.*, **61**, 6732 (2006).
20. D. L. Marchisio, A. A. Barresi and M. Garbero, *AIChE J.*, **48**, 2039 (2002).
21. J. Akroyd, A. J. Smith, L. R. McGlashan and M. Kraft, *Chem. Eng. Sci.*, **65**, 1915 (2010).
22. Z. Li, J. Kessel, G. Grünewald and M. Kind, *Drying Technol.*, **31**, 1888 (2013).
23. A. Delafosse, M.-L. Collignon, S. Calvo, F. Delvigne, M. Crine, P. Thonart and D. Toye, *Chem. Eng. Sci.*, **106**, 76 (2014).
24. M. Gresch, R. Brügger, A. Meyer and W. Gujer, *Environ. Sci. Technol.*, **43**, 2381 (2009).
25. A. Nørregaard, C. Bach, U. Krühne, U. Borgbjerg and K. V. Gernaey, *Chem. Eng. J.*, **356**, 161 (2019).
26. Y. Shah, B. G. Kelkar, S. Godbole and W. D. Deckwer, *AIChE J.*, **28**, 353 (1982).
27. S. Yang, S. Kiang, P. Farzan and M. Ierapetritou, *Processes*, **7**, 9 (2019).
28. M. Kim, S. Park, D. Lee, S. Lim, M. Park and J. M. Lee, *Chem. Eng. J.*, **395**, 125034 (2020).
29. F. Bezzo, S. Macchietto and C. Pantelides, *AIChE J.*, **49**, 2133 (2003).
30. W. Zhao, A. Buffo, V. Alopaeus, B. Han and M. Louhi-Kultanen, *AIChE J.*, **63**, 378 (2017).
31. H. Hatzantonis, A. Goulas and C. Kiparissides, *Chem. Eng. Sci.*, **53**, 3251 (1998).
32. D. L. Marchisio and R. O. Fox, *J. Aerosol Sci.*, **36**, 43 (2005).
33. D. L. Marchisio, R. D. Vigil and R. O. Fox, *J. Colloid Interface Sci.*, **258**, 322 (2003).
34. D. L. Marchisio, R. D. Vigil and R. O. Fox, *Chem. Eng. Sci.*, **58**, 3337 (2003).
35. R. G. Gordon, *J. Math. Phys.*, **9**, 655 (1968).
36. L. Metzger and M. Kind, *Chem. Eng. Sci.*, **169**, 284 (2017).
37. A. Shamiri, M. A. Hussain, F. S. Mjalli and N. Mostoufi, *Chem. Eng. J.*, **161**, 240 (2010).
38. R. Fan, Ph.D. thesis, Iowa State University, Ames, IA (2006).
39. T. J. Niemi, M.S. thesis, Aalto University (2012).
40. C. Chen, Q. Dai and H. Qi, *Chem. Eng. Sci.*, **141**, 8 (2016).
41. H. Qi, F. Li, B. Xi and C. You, *Chem. Eng. Sci.*, **62**, 1670 (2007).
42. Q. Zhou and J. Wang, *Chem. Eng. Sci.*, **122**, 637 (2015).
43. F. Vejahati, N. Mahinpey, N. Ellis and M. B. Nikoo, *Can. J. Chem. Eng.*, **87**, 19 (2009).
44. E. Esmaili and N. Mahinpey, *Adv. Eng. Software*, **42**, 375 (2011).
45. E. Ghadirian and H. Arastoopour, *Powder Technol.*, **288**, 35 (2016).

Supporting Information

A two-way coupled CFD-DQMOM approach for long-term dynamic simulation of a fluidized bed reactor

Minjun Kim, Kyoungmin Lee, Youngseok Bak, and Jong Min Lee†

School of Chemical and Biological Engineering, Institute of Chemical Processes, Seoul National University, Gwanak-ro 1, Gwanak-gu, Seoul 08826, Korea

(*Received 18 June 2020 • Revised 21 September 2020 • Accepted 28 October 2020*)

1. Mesh Test

The number of nodes was determined to be 307,776 based on the mesh robustness test, in which the number of nodes was increased until a further increase in the number of nodes exerted no effect on the results in the CFD-hydrodynamics model (see Fig. S1).

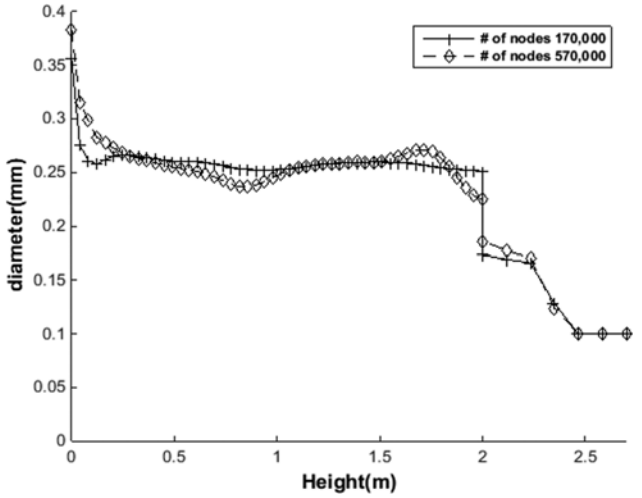

Fig. S1. d_{32} along the height as a function of number of nodes between 170,000 and 570,000.

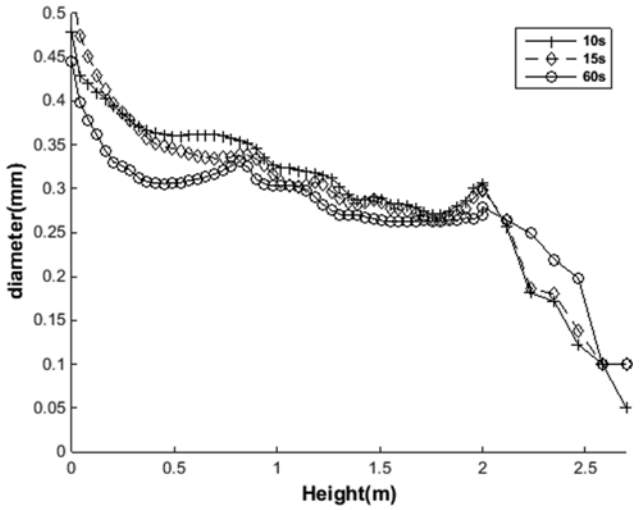

Fig. S2. d_{32} (Sauter mean diameter) along height for flow updating intervals of 10, 15, and 60 s models.

2. Flow Update Interval

A sensitivity analysis was performed to determine the time interval required to update the flow information. Fig. S2 shows d_{32} along height plot for flow updating intervals of 10, 15, and 60 s.

3. Configurations of 84-, 228-, and 348-zone Models

Fig. S3 shows the side views of the 84-, 228-, and 348-zone models.

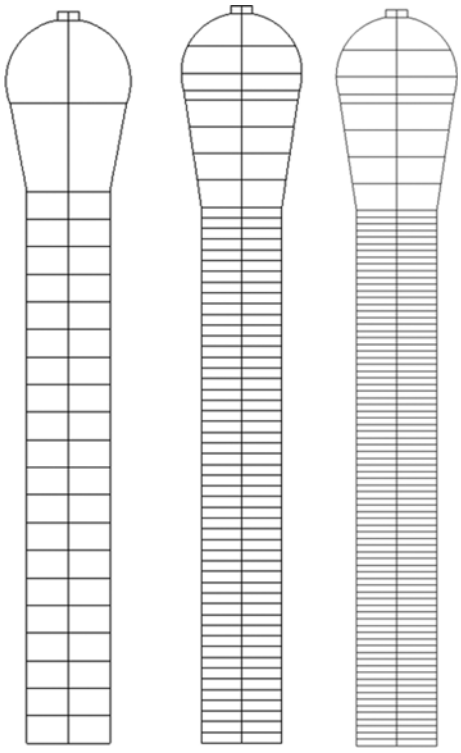

Fig. S3. Side views of 84-, 228-, and 348-zone models.